RESEARCH PAPER

Photocatalytic outcomes for methylene blue degradation from CTAB mediated mesoporous ZnS synthesized by an insoluble precursor in ethanol medium

Ramin Houshmand, Hosein Banna Motejadded Emrooz*

Nanotechnology Department, School of New Technologies, Iran University of Science and Technology, Tehran, Iran

ARTICLE INFO

ABSTRACT

The aim of the present study is to demonstrate how mesoporous nanostructures of zinc sulfide (ZnS) precipitate in an ethanol medium, in spite of negligible solubility of sodium sulfide (Na2S), which performs as a sulfur precursor. On the following, the role of such synthesis method on the photocatalytic behavior of ZnS mesoporous nanostructures is investigated. Characterization of the synthesized samples was carried out through X-ray diffraction patterns (XRD), Furrier transformation infrared spectroscopy (FTIR), transmission electron microscopy (TEM), diffuse reflectance spectroscopy (DRS), field emission scanning electron microscopy (FESEM) and N2 adsorption – desorption analysis. Formation of NaNO3 in assistance with negligible solubility of Na2S in ethanol enhances the stability of ZnS nanoparticles. Besides, formation of NaNO3 as well as sonication process can induce mesopores in the ZnS nanoparticles. Changes in the critical micelle concentrations (CMCs) of CTAB had impacts either in the lattice properties or in the textural structure of the mesopores of the synthesized samples. An attempt was made to explain how enhancement of CMCs values led to decrease in crystallite size and subsequently increase in lattice strain. The photocatalytic behavior and the adsorption capacity of the ZnS mesoporous structures were studied through methylene blue degradation from aqueous solution. It was found that adsorption capacity and photocatalytic efficiency of the synthesized samples were improved by modification of CMC values of CTAB. Findings were in line with the band gap energy values and water droplet contact angle measurements. This study is finalized by explaining how the synthesized photocatalysts remove contaminations under ultraviolet irradiation.

How to cite this article

INTRODUCTION

By publishing the first reports on the synthesizing of porous silica networks, mesoporous structures have attracted a lot of scientific and industrial attentions. Compared to other nanostructures (including no pores) with the same size and dimensions, mesoporous structures possess a higher surface area, better stability, numerous atoms on the surface and better activity. In fact, by supplying a higher surface area, mesoporous structures can provide more reactive sites resulting in a promoted chemical activity [1- 6]. These features have an outstanding role in the effectiveness of these materials in catalytic and biomedical applications such as drug delivery, removing contaminations from environments, water and wastewater purification, gas detection sensors, and solar energy conversion [7- 10].

Zinc sulfide is an inorganic non-toxic semiconductor belonging to group II-VI semi-conductors [11- 13]. Properties such as wide direct band gap and rapid formation of electron-hole pairs on the surface have made ZnS a critical element

in optoelectronic instruments such as blue light emitting diodes, solar cells and field emission devices [14- 16]. ZnS band gap energy, depending on its crystalline structure, can be 3.8 and 3.6 eV [12] for hexagonal (wurtzite) and cubic (sphalerite) phases, respectively. Due to various applications, an assortment of ZnS nanoparticles such as nanospheres, nanorods, thin films and mesoporous structures have been synthesized so far [17- 28]. In 1989, Lippens and Lannoo presented the first theory to study zinc sulfide nanoparticles, named small crystallites by the authors [29]. As time passed the knowledge for the synthesis of ZnS nanostructure increased. For instance, Gedanken et al. synthesized zinc sulfide nanoparticles through a sonochemistry method for the first time. Although the final samples were strongly agglomerated. In order to solve this problem, polyvinylpyrrolidone was used to stabilize the synthesized nanoparticles. Cao et al. prepared ZnS nanotubes using CS_2 and Triton X-100 as sulfide ions source and surfactant agent, respectively [30, 31].

Due to the considerable efficiency in removing organic pollutants from water, the synthesis of zinc sulfide mesoporous structures has been of a significant interest for abundant research studies [32, 33]. In some of these reports, the synthesis procedure contains either hard or soft templates. Structure directing agents such as P123, F127 and ODA were used in the synthesis procedure. In some studies, despite using no template, mesopores has been induced to ZnS nanostructures. More studies have been performed on synthesizing ZnS through template assistance than other methods [32- 38].

Synthesis of zinc sulfide mesoporous structures was initially introduced in the early 21st century, albeit weak results were reported at first. In the early stages, a low surface area and poor distribution of narrow pores were reported [39]. Primary research results proposed synthesis methods which cost a lot of time, so further research was needed to understand whether facile and effective methods can be designed to produce similar results. Nevertheless, results were improved and researchers employed facile hydrothermal methods. In 2003, Ranna et al. reported an ultrasound mediated synthesis method for ZnS mesoporous structure with mean pore diameter and specific surface area of the 28 Å and 210 m^2g^{-1}, respectively [40]. The highest reported specific surface area of this compound has been around 350 m^2g^{-1} up to now. Zhang et al. employed a co-template method to

synthesize mesoporous structures of ZnS [41]. Furthermore, auxiliary agents such as alkanols and polymers took part in some studies [42, 43]. Yun-Pei et al. examined outcomes of time-dependent sonication and solvent type effect on photocatalytic efficiency of ZnS mesoporous structures. They reported that long-term use of ultrasonic irradiation could prevent pores to remain huge [44]. Mehta et al. calculated size of ZnS monodisperses in aqueous solution and found that formation of ZnS nanoparticles in aqueous solution depends on CTAB concentration [45].

It appears that remarkable investigations have been accomplished to synthesize and characterize ZnS mesostructures. Research activities which, although literally outstanding, are not nevertheless terminated. One of the main challenges remained unsolved is the synthesis of ordered mesoporous ZnS structure which comes from the by-product of the synthesis reaction and also from the high rate of ZnS synthesis reaction. Any synthesis approach with low rate of reaction may therefore be suitable for resolving this challenge. For reducing the rate of the synthesis reaction, use of a weak solvent media which one or both of the precursors (Zn and S) is (are) weak soluble in it can be helpful. In the present work, ethanol, as a weak solvent for Na_2S (S precursor), has been selected for this purpose. Therefore, the first objective of this study is to clarify how ZnS nanoparticles could precipitate in the ethanol solvent despite the dissolution limit of sodium nitrate (Na_2S) for ZnS nanoparticles. The influence of such limited solubility and also the different concentrations of CTAB micelles which direct agent on the synthesized mesoporous has been investigated. Adsorption and photocatalytic behavior of ZnS mesoporous compounds for degradation of methylene blue have also been investigated.

EXPERIMENTAL PROCEDURES
Materials and Synthesis Process

All chemicals and reagents were of analytical grade and used as received without any further purification. Zinc nitrate hexahydrate (Zn $(NO_3)_2.6H_2O$) and sodium sulfide pentahydrate ($Na_2S.5H_2O$) were purchased from Dae Jung chemical company (South Korea). Cetyl tri methyl ammonium bromide (CTAB) was purchased from Merck Company. Deionized water and absolute ethanol (more than 99.8 %) were used in both synthesis and washing procedures. In a typical

synthesis, 350 mg of sodium sulfide pentahydrate ($Na_2S.5H_2O$) was dispersed in 20 ml of ethanol. Then, the mixture was transferred into ultrasonic wave generator device containing 610 mg of zinc nitrate hexahydrate in 20ml of ethanol and irradiated by an internal light source under 280 W for 5 min. During ethanol washing process, the precipitated powder was separated and labeled as ZS-EtoH. The procedure for another sample labeled as ZS-H_2O was the same but one modification in washing process, in that way, later sample was washed with deionized water in addition to ethanol. Other samples were synthesized using different amounts of CTAB in the same procedure. Values of 0.5, 1, 2 and 3 CMC of CTAB were added to the synthesis media of samples ZS-H_2O-0.5, ZS-H_2O-1, ZS-H_2O-2 and ZS-H_2O-3, respectively. The obtained samples were washed by ethanol and water at the end of the synthesis procedure. The washing process was performed before drying at temperature of 35°C. The obtained samples were placed in an oven and dried at temperature of 63°C during 4 hours.

Characterization

Normal angle X-ray diffraction patterns were recorded on a Philips (Netherland) PW1730 diffractometer with Cu Kα (λ =1.54 Å) radiation. Field emission scanning electron microscopy (FESEM) was carried out on a MIRA\\TESCAN (Czech) at an acceleration voltage of 30 kV. N_2 adsorption-desorption isotherms were recorded on a BELSORP mini II sorption analyzer equipment at a liquid nitrogen temperature of 77 K. Samples were degassed at 150°C for 6 h before all measurements. Fourier transformation infrared

(FTIR) spectroscopy in the range of 500 to 4000 cm^{-1} was performed for all specimens, using a 8400s Shimadzo model device. Diffuse reflectance spectroscopy (DRS) was performed on a Shimadzu (Japan) UV-2550 using barium sulfate as the source. UV-Vis spectra of MB solutions before and after photocatalytic degradation were recorded on a Shimadzu (Japan) 1700 spectrophotometer. Transmission electron microscopy (TEM) images obtained from a 200 kv Philips CM200 instrument.

Photocatalytic and Adsorption Evaluations

The adsorption capacity and photocatalytic behavior of synthesized mesoporous ZnS nanoparticles were evaluated by degradation of methylene blue ($C_{16}H_{18}ClN_3S.xH_2O$ (x=2–3)) from aqueous solution. For doing so, 20 mg of each specimen with 10 ml of MB solution were mixed together. The adsorption testing was performed in a dark room while stirring for 30 min. Photocatalytic activities were evaluated under three (8 W) UV lamp irradiation with maximum emission of 254 nm, when all samples were located 30 cm lower than the lamps and stirring for 30 min. In order to measure the water droplet contact angle of the synthesized ZnS nanoparticles, the samples were under pressure to form a compact of them. The contact angle of the ZnS nanoparticles were specified by values of the angle between the surface of the nanoparticles and the water droplets.

RESULTS AND DISCUSSION

Formation Mechanism of ZnS Nano Crystallites

ZS-EtoH and ZS-H_2O samples were synthesized employing Zn $(NO_3)_2$ and Na_2S as precursors in an ethanol media through a hydrothermal procedure.
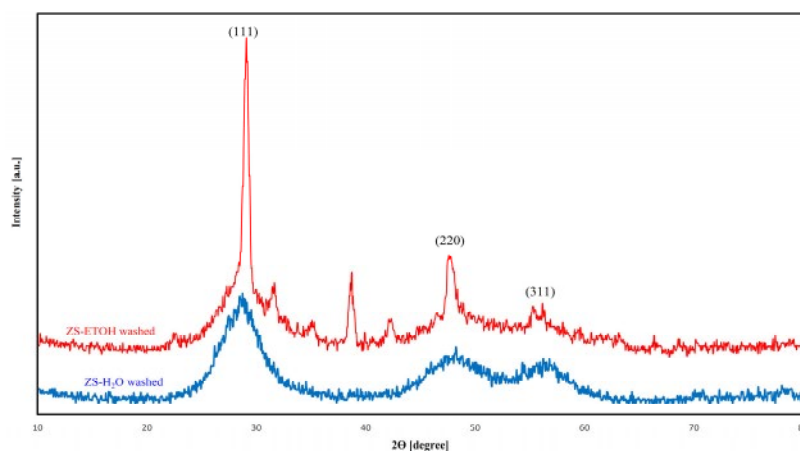

Fig. 1. XRD spectra of the synthesized ZnS nanoparticles using no surfactant agent.

The synthesis process of these two samples were quite similar and the only difference was the method of washing. Sample ZS-EtoH was only washed with ethanol while the other one was washed with ionized water after washing with ethanol. XRD patterns of these two specimens (Fig. 1) clearly show the formation of ZnS crystallites. Distinct broad diffraction peaks at $2\Theta = 28.9$, 47.7 and 56.7 are appeared due to reflection from the (111), (220) and (311) planes, respectively. These results indicate that the crystalline structures of these samples are in good accordance with simple cubic zinc sulfide (Zinc blende) with lattice constant of 5.41 Å (JCPDS card no. 05-0566). Besides, the presence of the $NaNO_3$ by-product can be distinguished in the ZS-EtOH specimen pattern by strong and sharp peaks at 31.7 and 38.6 degrees. This reveals a simultaneous precipitating of supersaturated sodium nitrate with ZnS nanoparticles during synthesis process. Weak solubility of sodium nitrate in ethanol (0.029 g in 100 ml of absolute ethanol at ambient temperature [40]) can justify remaining of $NaNO_3$ in the final structure of ZS-EtOH specimen. However for the specimen washed by ionized water, no sign of $NaNO_3$ precipitation is obtained due to high solubility of this inorganic salt in water (85 g in 100 ml water at ambient temperature [40]). In fact, water eliminated $NaNO_3$ from this specimen. It can be concluded that the bonds between the sodium nitrate molecules and zinc sulfide are broken down against the attraction force of water molecules. In ethanol atmosphere, these bonds exhibit greater resistance. They are unlikely to break and join ethanol molecules.

Fig. 1s shows FTIR spectra of ZnS specimens synthesized using neither template nor surfactant agent. With some perversion, separated bonds at 670, 980 and 1100 cm^{-1} are due to Zn-S stretching. Broad bands which can be seen for both specimens around 1625 and 3440 cm^{-1} are attributed to O-H stretching. Also, sharp peaks at 1379 cm^{-1} and 1789 cm^{-1} are related to the N-O suspension bands at the surface of the ZS-EtOH sample [46]. The appearance of N-O bands in FTIR results is another sign for the presence of $NaNO_3$ in the final structure of ZS-EtOH sample which indicates the insolubility of this salt in ethanol solvent.

FE-SEM micrographs of ZS-EtOH, Fig. 2, shows the formation of spherical nanoparticles with diameters of about 50 nm. Agglomeration of the synthesized nanoparticles can also be seen in this micrograph which is a sign for high surface energy of the particles. Also, this micrograph demonstrates the presence of porosities in the range about 25-100 nm in the agglomerated sample.

Considering the limited solubility of sodium sulfide, sulfur ions have a very low saturation point in ethanol, therefore, much smaller amount of sulfur ions will be present in the reaction of sulfide precipitation. In other words, the limited decomposition of sodium sulfide reduces the presence of sulfur ions in the medium, and therefore, the probability of zinc sulfide formation will be negligible. However, the results show that despite the very low solubility of sodium sulfide, zinc sulfide precipitates in ethanol. To find out the reason for the formation of zinc sulfide despite the negligible solubility of sodium sulfide, the mechanism of by-product formation (sodium nitrate) should be considered. At the beginning of zinc sulfide precipitating process, zinc nitrate is completely dissolved in ethanol. Therefore, there are enough nitrate and zinc ions in ethanol solvent. On the other hand, given that sodium sulfide is insoluble in ethanol, it is expected that S^{2-} and Na^+ ions will not be present in the synthesis media. It should be noted that the solubility of Na_2S in ethanol practically is not zero, and a little bit amount of this salt is dissolved in ethanol. Dissolution of this limited amount of Na_2S helps sulfur ions reach their saturation level in ethanol quickly. As can be seen in Fig. 2s, due to high solubility of $Zn(NO_3)_2$ in ethanol, Zn^{2+} and nitrate ions are homogenously
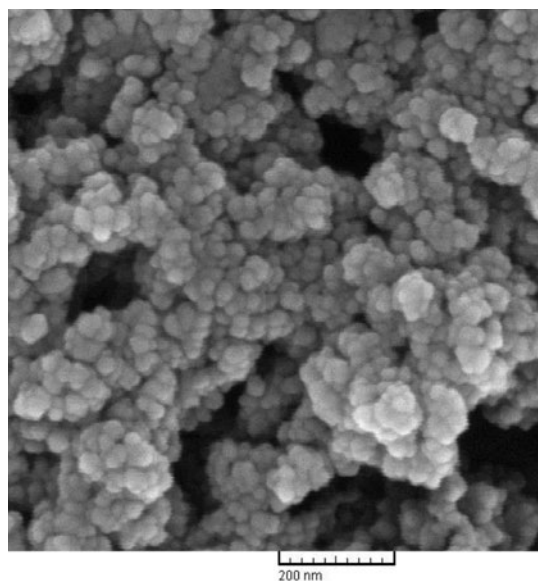

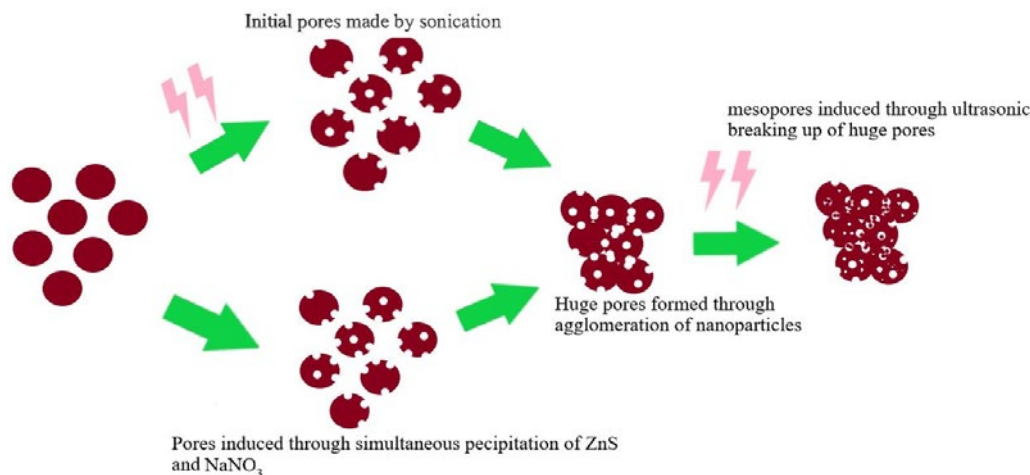Fig. 2. FE-SEM micrograph of specimen ZS-EtoH.

Fig. 3. Role of sonication in forming of mesoporous structures.

present at all the points of the media. Eminent presence of Zn^{2+} and NO_3^{1-} ions make S^{2-} and Na^+ join them fast. In this way, ions with opposite charge react with each other to constitute $NaNO_3$ and ZnS solids. Hence, saturation of sulfur ions around Na_2S will be broken up, and, as might be expected, Na_2S dissolution and S^{2-} are continued until resaturation of the solution. This is how Na_2S dissolves in ethanol medium in spite of its negligible solubility.

In addition, ultrasonic waves have an outstanding role in dissemination of sulfur ions from saturated zone near the Na_2S precursor. As shown in Fig. 2s, ultrasonic waves by applying mechanical force can disperse sulfur ions in solution and, in turn, the concentration of S^{2-} ions around Na_2S decreases faster which results in more dissolution of Na_2S.

Porosity formation in CTAB assisted synthesized ZnS particles

During CTAB assisted synthesis of ZnS nanoparticles, ultrasonic waves, synchronously precipitation of supersaturated $NaNO_3$ with ZnS particles, and assistance of CTAB molecules are three major sources to explain how mesoporous structures are formed in ZnS specimens. Fig. 3, schematically illustrates how ultrasonic waves induce porosities in the final structures. During ultrasonic irradiation, emission of these beams between floating components produces a lot of heat on the surface of ZnS nanoparticles. The combination of mechanical and thermal stresses can overcome the high yield strength of ZnS nanocrystallites to establish initial pores. It is worth

mentioning that the high yield strength of ZnS nanoparticles (about 5 GPa) [11] originates from its single crystalline nature. Elimination of $NaNO_3$ from ZnS-$NaNO_3$ composite which occurs during deionized water washing is another source for imposing porosities in the ZnS structure. $NaNO_3$ formation, in addition to its role in the synthesis of zinc sulfide nanoparticles, also affects the formation of irregular mesoporous structures. This inorganic salt, which is deposited along the ZnS precipitations occupies places susceptible to form fine pores. Finally, this lateral product is removed from ZnS nanostructure by water extraction while imprints of narrow pores emerge into the structure. Because of the agglomeration of sodium nitrate constitutes along with concurrent precipitating of $NaNO_3$ with ZnS particles, removal of this by-product induces irregularity into final mesoporous structure. Besides, difference between radius of the occupied spaces and the initial pores enhances irregularity. Agglomeration may obliterate some of these initial pores. Agglomeration can also merge initial pores to form larger ones beyond the mesopore range, (Fig. 2). As shown in Fig. 3, ultrasonic waves can break down huge pores into smaller ones in order to boost creating mesopores in final structure.

CTAB effects on ZnS lattice properties

The results obtained from the characterization analyses show that the change in critical micelle concentration of CTAB affects the ZnS crystalline structure. Normal angle XRD patterns of template assisted synthesized mesoporous ZnS nanoparticles are shown in Fig. 4. The surfactant

free specimen (ZS-H$_2$O) is also included in this analysis to authenticate the elimination of template agent. Three distinct peaks which can be seen for all specimens at 28.9, 47.7 and 56.7 are attributed to (111), (220) and (311) planes of cubic ZnS phase (zinc blend), respectively (JCPDS card no. 05-0566). Broadening of the ZnS characteristic peaks by increase in CTAB concentration in the synthesis media suggests tangible decrease in the size of ZnS crystallites. Crystallites size and lattice strains for ZnS mesoporous particles given from Williamson-Hall plotting is tabulated in Table 1. Williamson-Hall expression is as follows:

$$\beta \cos \theta = \frac{0.9\lambda}{D} + 4\varepsilon \sin \theta$$

where β is full width at half maximum (FWHM), Ө is Bragg angle of {hkl} reflections, λ is wavelength of X-ray irradiation, D and ε are crystallite size and lattice strain, respectively [47]. By plotting values of β cos (Ө) against sin (Ө), a straight line will be obtained with vertical axis intercept equal to 0.9λD^{-1} and a slope equal to 4ε. Application of Williamson-Hall plotting implies that ZnS-H$_2$O-3 possesses smaller crystallites than other counterparts. Changing procedure of lattice parameters for mesoporous ZnS specimens is shown in Fig. 5. As can be seen, increase in the critical micelle concentration of CTAB has led to reduction in the crystallite size and an increase in the lattice strain. Exterior surface of micelles and hydrophilic head of CTAB molecules are appropriate sites for ZnS nucleation (Fig. 3s). By increasing the number of CTAB molecules in the solvent, the number of suitable sites for zinc nucleation increases. More

Table 1. Amounts of lattice properties obtained from XRD patterns.

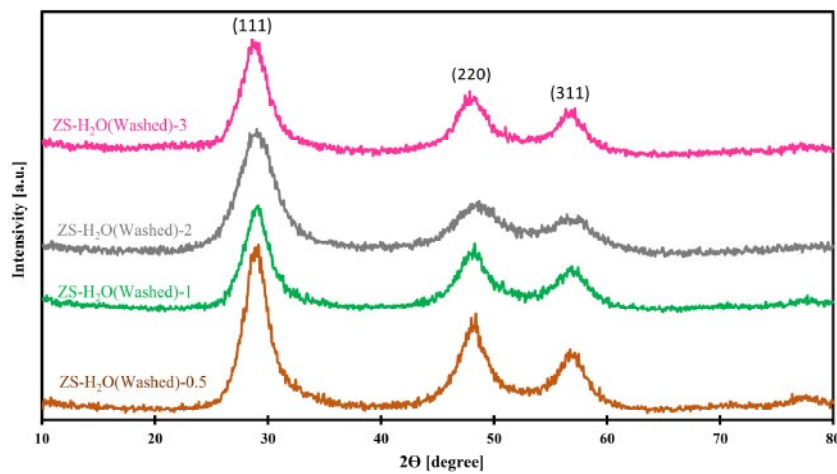| Samples	Crystallite size	Lattice strain ($\times 10^{-3}$)
ZS-H$_2$O	2.5	-2.5
ZS-H$_2$O-0.5	2.39	-3.16
ZS-H$_2$O-1	2.16	-3.19
ZS-H$_2$O-2	1.86	-3.71
ZS-H$_2$O-3	1.47	-4.135

Fig. 4. XRD patterns for synthesized samples using CTAB molecules as surfactant agent.
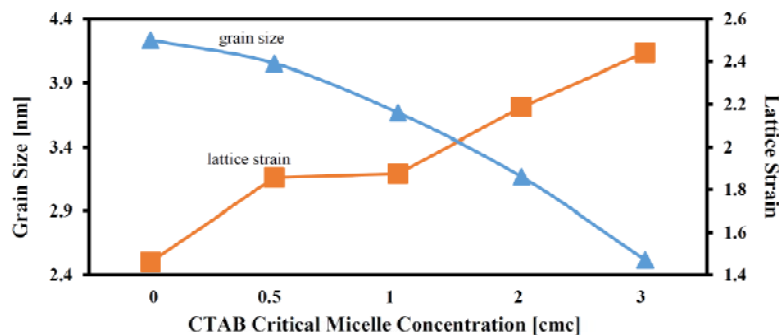

Fig. 5. Change process of lattice properties with increase in CMC values of CTAB.

suitable sites means that ZnS particles prefer nucleation to grow, as a consequence, more sulfur and zinc ions are involved in nucleation, and, therefore, less ions will participate in growth process which results in the reduction of crystallite size. In other words, an increase in CTAB critical micelle concentration reduces growth rate of ZnS crystallites and makes them remain smaller.

CTAB effects on the morphology of the ZnS particles

FTIR spectra were recorded for all the synthesized specimens to find out the effectiveness of the extraction template (different CMCs of CTAB), (Fig. 4s). Since no characteristic peaks of pure CTAB at 721, 2924, 960, 909, 2852 and 1490 cm^{-1} were detected, utilized washing method could be reliable. As can be seen, recognizable bands at around 670, 980 and 1100 cm^{-1} can be assigned to Zn-S stretching. Since vibration frequencies of O-H stretching and N-H stretching are overlapped at around 1620 and 3440 cm^{-1}, their distinction is not facile. Wide vibrational bands at 2920 and 2850 are attributed to C-H symmetrical and asymmetrical stretching mode due to remained surfactants on the surface of the specimens. As can be seen, the most intensified C-H bands belong to ZS-H_2O-0.5.

N_2 adsorption-desorption isotherms of the template extracted specimens are presented in Fig 6-a. According to IUPAC classification, all isotherms possess a hysteresis loop of type IV indicating existence of mesoporous structures. BET surface area, average pore diameters, and total pore volume of samples calculated using BJH method are provided in Table 2. Based on the results, adding more CTAB molecules to the ethanol solvent in order to exceed 1 CMC decreases special surface area of the synthesized samples. Increase in CMC also led to larger pores (average pore diameter) from 6 to 20 nm and total pore volume (Table 2 and Fig. 6-b). TEM images of ZS-H_2O-1 indicates formation of porous structures. (Fig 6-c). Sidim et al. reported that presence of a strong attraction between the surfactant agents and the solvent molecules causes delay in the formation of micelles [48]. So,

existence of a strong attraction between ethanol and hydrophilic heads of CTAB molecules can explain the mechanism of pore enlargement. This attraction is able to impose some delay in micelle formation. So, instead of joining together to form micelles, more surfactant molecules will remain in the solvent media. In that case, density of CTAB molecules improves which provides more approaching surfactant molecules to join
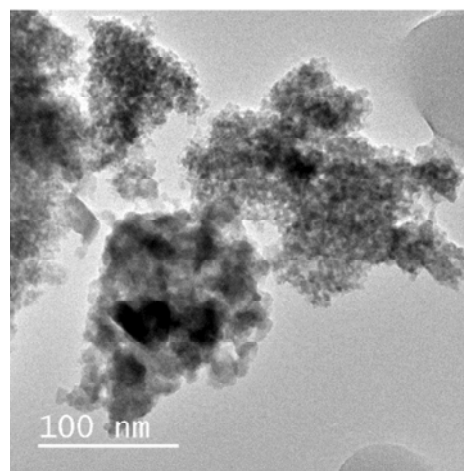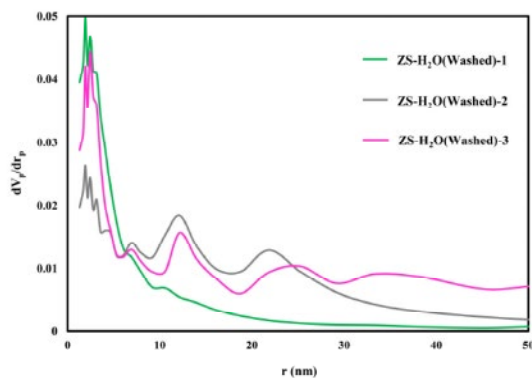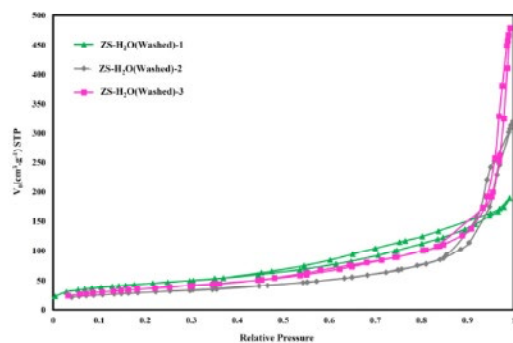

Table 2. Extracted data from N2 adsorption-desorption plotting.

Sample	APD [nm]	TPV[cm^3g^{-1}]	SSA [m^2g^{-1}]
ZS-H_2O-1	7.36	0.289	157.12
ZS-H_2O-2	17.52	0.46	104.85
ZS-H_2O-3	21.25	0.688	129.58

Fig. 6. (a) N2 adsorption-desorption, (b) Variation of the porosity radius & (c) TEM image of ZnS mesoporous structures.

pre-micellar assemblies, and, therefore, there is no need to separate all the surfactant molecules from solvent attraction. Such aggregations as pre-micellar assemblies are a by-product of rising density of surfactant molecules. Consequently two occurrences might happen:

1. Rather than joining to the pre-micellar assemblies, surfactant molecules are locked up into the micellar assemblies and enlarge them, so larger pores remain after surfactant extracting.
2. More aggregations may reach the CMC, so more micelles will be available in the solvent. Therefore, the possibility of micelle fusion increases which shapes the coarse-dimensioned

pores. Moreover, induced load of CTA$^+$ locked up inside the micelles can be in further assistance with fusion of micelles.

Photocatalytic behavior of ZnS mesoporous nanostructures

To determine the photocatalytic efficiency of the as-synthesized ZnS mesoporous structures, degradation of methylene blue from aqueous solution under UV irradiation was investigated. The highest degradation efficiency was recorded for ZS-H$_2$O-3 and ZS-H$_2$O-1 as compared to other specimens. In addition, surface adsorption capacities of ZnS mesoporous structures
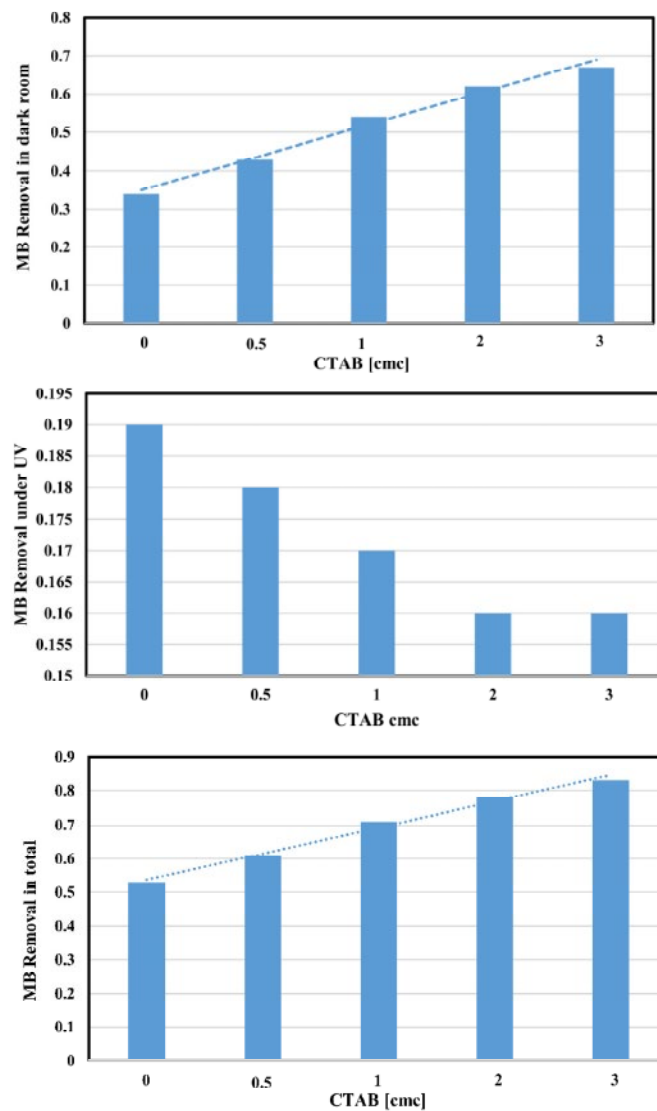

Fig. 7. (a) Adsorption, (b) photocatalytic behavior & (c) dye removal of the synthesized ZnS porous specimens from different CMC values of CTAB.

Table 3. Water droplet angle of synthesized samples.

Sample	Contact Angle [degree]
ZS-H$_2$O	50.21
ZS-H$_2$O-0.5	51.49
ZS-H$_2$O-1	45.85
ZS-H$_2$O-2	38.56
ZS-H$_2$O-3	48.60

synthesized using different amount of template concentration are shown in Fig. 5s. The data about MB removal is after 30 minutes.

Photocatalytic and adsorption behavior of the synthesized mesoporous structures at different CMC values of CTAB are illustrated in Figs. (7-a) and (7-b), respectively. As can be seen, increase of CMC value improves adsorption and photocatalytic efficiency of the synthesized samples. Water droplet contact angle of ZnS mesoporous samples are tabulated on Table 3. Contact angle between sessile water droplets and free surface of ZnS nanoparticles can be calculated from Young-Laplace equation:

$$\Gamma_{sv} - \Gamma_{sl} = \Gamma_{lv}cos\theta$$

where Γ_{sv} denotes the solid–vapor interfacial energy, Γ_{sl} is the solid–liquid interfacial energy and Γ_{lv} is the liquid–vapor interfacial energy. So contact angle can be quantified by θ [52]. According to Young–Laplace equation, decrease in water droplet angle means more wettability on ZnS nanoparticles and more active sites for absorbing dye molecules from impregnated water. Therefore, the possibility of separating methylene blue molecules from aqueous solution and joining them to the ZnS nanoparticle

surface increases, and thus, more values of dye degradation for samples with smaller contact angle is desirable. Fig. 8 illustrates the compatibility between the results of the adsorption test and the water droplet contact angle of the ZnS mesoporous samples. As can be seen, by increasing the water droplet contact angle for ZnS mesoporous samples, the amount of methylene blue adsorption from aqueous solution has decreased. However, despite the bigger contact angle, ZS-H$_2$O-0.5 sample shows a higher adsorption capacity than ZS-H$_2$O sample. The increase in adsorption amount for sample ZS-H$_2$O-0.5 is due to the presence of C-H bands at the surface of this sample. Suspended C-H bands are likely to remain in the final structure due to the washing of samples with ethanol. As can be deduced from FTIR spectra for synthesized specimens, the largest number of C-H bands is related to ZS-H$_2$O-0.5. The attendance of C-H bands results in hydrophobic nature of the surface. This, in turn, decreases the effective surface area for adsorption of methylene blue. On the other hand, C-H bands present on the free surface of the samples prefer participating in organic reactions to the cations of methylene blue. Therefore, C-H bands exhibit more affinity to methylene blue molecules leading to more degradation of MB molecules from aqueous solution by ZS-H$_2$O-0.5.

The band gap energy for semiconductor materials is a function of different parameters such as crystallite size, surface defects and dangling bands. By reducing the crystallite size, quantum confinement effects lead to an increase in band gap energy [49]. However, it is expected that increase
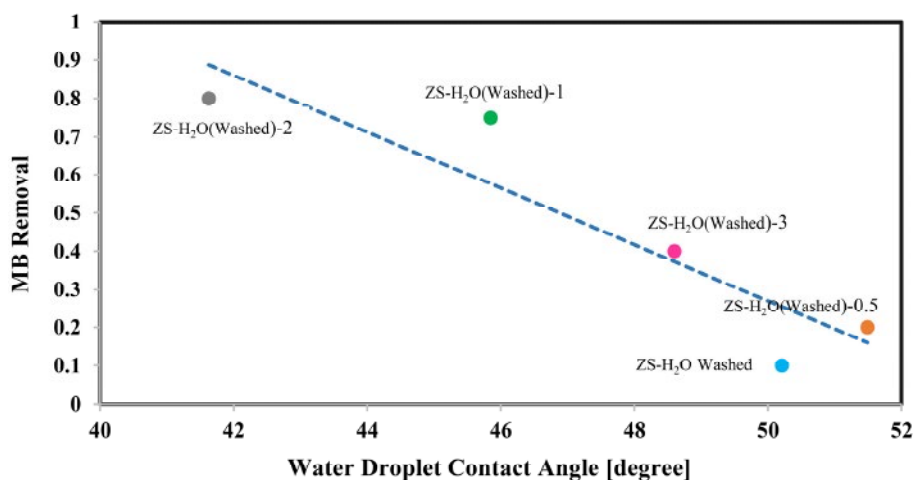

Fig. 8. Compatibility between the results of the adsorption testing and values of water droplet contact angle.

in grain boundaries area induce some levels of inter bands in the band structures of materials. Therefore, it is expected by increasing the critical micelle concentration of CTAB (reduction in the crystallite size), the absorption spectra of the synthesized samples are transfered to shorter wavelengths (referred to Fig. 5). Nevertheless, DRS spectra of the synthesized specimens (Fig. 9) indicates incompatibility with crystallite size of ZnS mesoporous structures. As can be seen, despite the effect of crystalline size, the maximum value for band gap energy is related to ZS-H$_2$O-2 specimen. The precise amount of band gap energy can be calculated using Tauc equation:

$$\alpha h \vartheta = A \left(h \vartheta - E_g \right)^n$$

where A is a constant called the band tailing parameter, $h\vartheta$ is photon energy, E_g is allowed energy of the optical band gap which is dependent to the regularity in the structure, crystalline or amorphous, n=0.5 is valid for crystalline structures with allowed direct transition and n=2 is valid for amorphous structures with allowed indirect transition [50]. According to Fig. 6s, band gap energy obtained by Tauc plotting for ZS-H$_2$O-0.5, ZS-H$_2$O-1, ZS-H$_2$O-2 and ZS-H$_2$O-3 specimens is equal to 3.28, 3.32, 3.43 and 3.39 eV, respectively. Although these results do not match the crystallite size obtained from XRD patterns, it is being understood that surface defects play a more prominent role in the band gap energy of mesoporous structures than crystallite size. Regarding to high surface area of mesoporous

structures, surface properties in such structures are more impressive. On the other hand, from BJH analysis (Table 2), it was found that the highest surface area belongs to sample ZS-H$_2$O-1. The enhancement of surface area for this sample leads to more defects in the structures, so decrease in band gap energy values is to be expected. According to Table 2, surface area of the synthesized samples is in the order of ZS-H$_2$O-1 > ZS-H$_2$O-3 > ZS-H$_2$O-2 which is compatible with the sequence of band gap energy given from Tauc plotting, (Fig. 6s).

The value of band gap energy can determine which part of the light spectrum can be absorbed by the material (catalyst). Since semiconductor photocatalysts only absorb photons with energy equal to or greater than the band gap energy, the high band gap energy of ZS-H$_2$O-3 can justify weak photocatalytic response of this sample.

Effect of ultraviolet irradiation on the efficiency of ZnS mesoporous structures in removing pollution from aqueous solution is presented in Fig. 7s. It can be concluded that ultraviolet irradiation improved the amount of methylene blue degradation from the aqueous solution. Mechanism of photocatalytic reactions under ultraviolet irradiation is illustrated in Fig. 10. By absorbing the intensity of ultraviolet photons, in the case of energies equal to or greater than the band gap energy of ZnS nanoparticles, photocatalytic reactions will begin which result in the production of electron-hole pairs on the surface of ZnS nanoparticles. Due to irradiation of ultraviolet photons, ZnS nanoparticles in addition to being present in the solution as an electron donating agent, can absorb molecules that are in
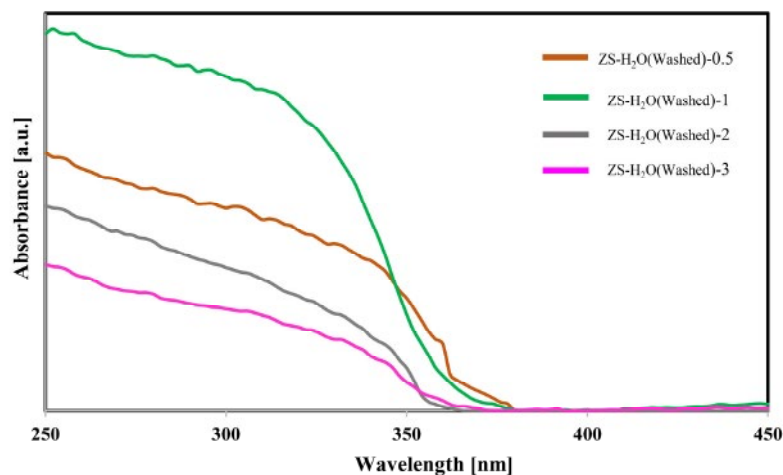

Fig. 9. Diffuse reflectance spectra of synthesized samples using different values of CTAB CMC.
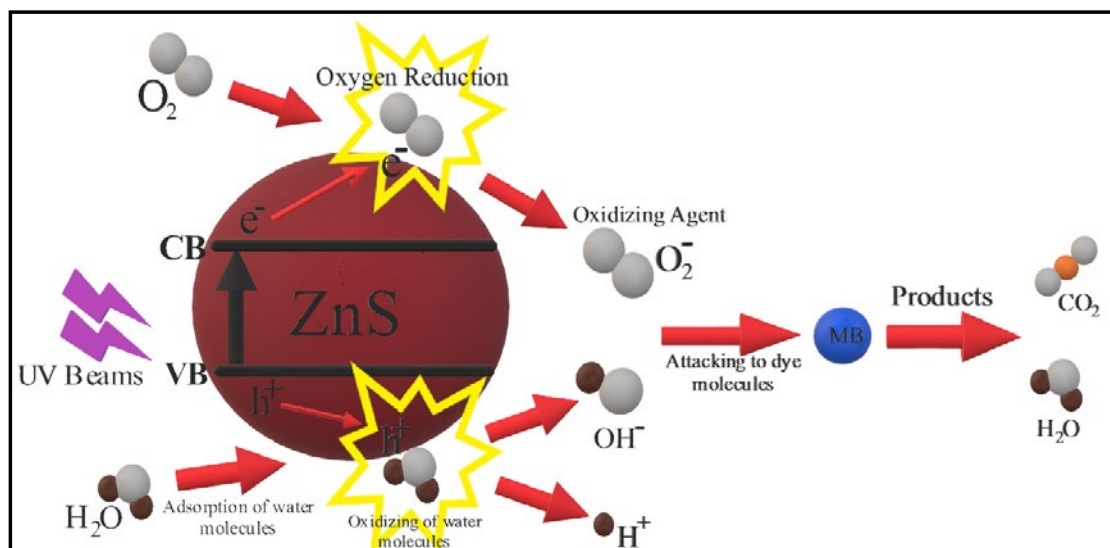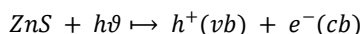
Fig. 10. Schematic illustration of redox reactions happening on the surface of ZnS nanoparticles under UV irradiation.

contact with the semiconductor. The following reaction represents the formation of electron-hole as oxidizing and reducing agents.

$$ZnS + h\vartheta \mapsto h^+(vb) + e^-(cb)$$

In the above reaction, "Cb" and "Vb" indicate conduction and valence band, respectively. Reduction of adsorbed oxygen molecules into oxidant radicals prevents electron-hole pairs to reconstruct [51]. Consequently, the accumulation of electron radicals results in their presence for removing pollutions from aqueous solution. Radiation of ultraviolet beams improves certain electrons from the valence band of zinc sulfide to its conduction band, so induced electrons move from the surface of the pores which can either react with surface defects or take part in some chemical reactions. During the MB degradation from aqueous solution, hydroxyl radicals formed within water or OH oxidation have the ability to emerge as the first oxidants. Radicals of OH⁻ will attack pollutants briskly, so, it can be said that OH⁻ radicals are the most important ones that are formed by photocatalyst.

CONCLUSION

According to the results, formation of a by-product called $NaNO_3$ in assistance of negligible solubility of Na_2S in ethanol supports precipitation of ZnS nanoparticles. Through providing more suitable sites for nucleation of ZnS nanocrystallites,

increase of critical micelle concentration of CTAB made improvement in nucleation rate, consequently, the dimensions of nanocrystallites decreased. Enhancement of cmc value of CTAB improved adsorption capacity of the samples obtained. It was also demonstrated that values of adsorption capacity for the synthesized samples were in accordance with amounts of water droplet contact angle. Increase in critical micelle concentration of CTAB in synthesis media indicates improvement in photocatalytic efficiency under UV lights by the ZnS mesoporous structures.

CONFLICT OF INTEREST

The authors declare no conflict of interest.

SUPPLEMENTARY MATERIAL

The Supplementary Material for this article can be found online at: http://nanochemres.org/.

REFERENCES

[1] Zhang W-H, Shi J-L, Chen H-R, Hua Z-L, Yan D-S. Synthesis and Characterization of Nanosized ZnS Confined in Ordered Mesoporous Silica. Chemistry of Materials. 2001;13(2):648-54.

[2] Schüth F. Non-siliceous Mesostructured and Mesoporous Materials†. Chemistry of Materials. 2001;13(10):3184-95.

[3] Fukuoka A, Kimura J-i, Oshio T, Sakamoto Y, Ichikawa M. Preferential Oxidation of Carbon Monoxide Catalyzed by

Platinum Nanoparticles in Mesoporous Silica. Journal of the American Chemical Society. 2007;129(33):10120-5.

[4] Koshida N, Ozaki T, Sheng X, Koyama H. Cold Electron Emission from Electroluminescent Porous Silicon Diodes. Japanese Journal of Applied Physics. 1995;34(Part 2, No. 6A):L705-L7.

[5] Lehmann V, Gösele U. Porous silicon formation: A quantum wire effect. Applied Physics Letters. 1991;58(8):856-8.

[6] Lowell S, Shields JE, Thomas MA, Thommes M. Characterization of porous solids and powders: surface area, pore size and density: Springer Science & Business Media; 2012.

[7] Lowell S, Shields JE. Powder surface area and porosity: Springer Science & Business Media; 2013.

[8] Yuan C, Li J, Hou L, Zhang X, Shen L, Lou XWD. Ultrathin Mesoporous NiCo2O4Nanosheets Supported on Ni Foam as Advanced Electrodes for Supercapacitors. Advanced Functional Materials. 2012;22(21):4592-7.

[9] Davis ME. Ordered porous materials for emerging applications. Nature. 2002;417(6891):813-21.

[10] Su B-L, Sanchez C, Yang X-Y. Hierarchically structured porous materials: from nanoscience to catalysis, separation, optics, energy, and life science: John Wiley & Sons; 2012.

[11] Mandal T, Maiti PK, Dasgupta C. Mechanical properties of ZnS nanowires and thin films: Microscopic origin of the dependence on size and growth direction. Physical Review B. 2012;86(2).

[12] Isshiki M, Wang J. Wide-Bandgap II-VI Semiconductors: Growth and Properties. Springer Handbook of Electronic and Photonic Materials: Springer International Publishing; 2017. p. 1-.

[13] Kisch H. Semiconductor Photocatalysis for Chemoselective Radical Coupling Reactions. Accounts of Chemical Research. 2017;50(4):1002-10.

[14] Zhou R. Semiconductor Photocatalysis: Mechanism, Photocatalytic Performances and Lifetime of Redox Carriers. 2017.

[15] Fu A, Gu W, Boussert B, Koski K, Gerion D, Manna L, et al. Semiconductor Quantum Rods as Single Molecule Fluorescent Biological Labels. Nano Letters. 2007;7(1):179-82.

[16] Zhu Y-C, Bando Y, Xue D-F, Golberg D. Nanocable-Aligned ZnS Tetrapod Nanocrystals. Journal of the American Chemical Society. 2003;125(52):16196-7.

[17] Fang XS, Bando Y, Shen GZ, Ye CH, Gautam UK, Costa PMFJ, et al. Ultrafine ZnS Nanobelts as Field Emitters. Advanced Materials. 2007;19(18):2593-6.

[18] Ke W, Stoumpos CC, Logsdon JL, Wasielewski MR, Yan Y, Fang G, et al. TiO2–ZnS Cascade Electron Transport Layer for Efficient Formamidinium Tin Iodide Perovskite Solar Cells. Journal of the American Chemical Society. 2016;138(45):14998-5003.

[19] Hu Y, Fu A, Miao Z, Zhang X, Wang T, Kang A, et al. Fluorescent ligand fishing combination with in-situ imaging and characterizing to screen Hsp 90 inhibitors from Curcuma longa L. based on InP/ZnS quantum dots embedded mesoporous nanoparticles. Talanta. 2018;178:258-67.

[20] Li J, Kessler H, Soulard M, Khouchaf L, Tuilier M-H. Nanosized Zinc Sulfide Obtained in the Presence of Cationic Surfactants. Advanced Materials. 1998;10(12):946-9.

[21] Dong S, Li C, Li Z, Zhang L, Yin L. Mesoporous Hollow Sb/ZnS@C Core-Shell Heterostructures as Anodes for High-Performance Sodium-Ion Batteries. Small. 2018;14(16):1704517.

[22] Tiemann M, Marlow F, Brieler F, Lindén M. Early Stages of ZnS Growth Studied by Stopped-Flow UV Absorption Spectroscopy: Effects of Educt Concentrations on the Nanoparticle Formation. The Journal of Physical Chemistry B. 2006;110(46):23142-7.

[23] Tiemann M, Marlow F, Hartikainen J, Weiss Ö, Lindén M. Ripening Effects in ZnS Nanoparticle Growth. The Journal of Physical Chemistry C. 2008;112(5):1463-7.

[24] Hamad S, Cristol S, Catlow CRA. Simulation of the Embryonic Stage of ZnS Formation from Aqueous Solution. Journal of the American Chemical Society. 2005;127(8):2580-90.

[25] Jang J, Yu C, Choi S, Ji S, Kim E, Lee J. Topotactic synthesis of mesoporous ZnS and ZnO nanoplates and their photocatalytic activity. Journal of Catalysis. 2008;254(1):144-55.

[26] Hamad S, Woodley SM, Catlow CRA. Experimental and computational studies of ZnS nanostructures. Molecular Simulation. 2009;35(12-13):1015-32.

[27] Fischereder A, Martinez-Ricci ML, Wolosiuk A, Haas W, Hofer F, Trimmel G, et al. Mesoporous ZnS Thin Films Prepared by a Nanocasting Route. Chemistry of Materials. 2012;24(10):1837-45.

[28] Feigl C, Russo SP, Barnard AS. Safe, stable and effective nanotechnology: phase mapping of ZnS nanoparticles. Journal of Materials Chemistry. 2010;20(24):4971.

[29] Lippens PE, Lannoo M. Calculation of the band gap for small CdS and ZnS crystallites. Physical Review B. 1989;39(15):10935-42.

[30] Cui X, Mao S, Liu M, Yuan H, Du Y. Mechanism of Surfactant Micelle Formation. Langmuir. 2008;24(19):10771-5.

[31] Lv R, Cao C, Guo Y, Zhu H. Preparation of ZnS nanotubes via surfactant micelle-template inducing reaction. Journal of Materials Science. 2004;39(5):1575-8.

[32] Muruganandham M, Kusumoto Y. Synthesis of N, C Codoped Hierarchical Porous Microsphere ZnS As a Visible Light-Responsive Photocatalyst. The Journal of Physical Chemistry C. 2009;113(36):16144-50.

[33] Li J, Zhao X, Yan C. Synthesis and characterization of mesoporous zinc sulfide by surfactant-assisted templating process. Materials Letters. 2006;60(23):2896-9.

[34] Zhou Z, Li Y, Liu L, Chen Y, Zhang SB, Chen Z. Size- and Surface-dependent Stability, Electronic Properties, and Potential as Chemical Sensors: Computational Studies on One-dimensional ZnO Nanostructures. The Journal of Physical Chemistry C. 2008;112(36):13926-31.

[35] Jang JS, Kim ES, Choi SH, Kim DH, Kim HG, Lee JS. Synthesis, electronic property and photocatalytic applications of mesoporous cobalt-doped ZnS and ZnO nanoplates. Applied Catalysis A: General. 2012;427-428:106-13.

[36] He Q, Cao Y, Miao Z, Ren X, Chen J. Estimation of Pores Distribution in Lignite Utilizing Hg, H2O, CO2, and N2 as Molecular Probes. Energy & Fuels. 2017;31(12):13259-65.

[37] Petkovich ND, Stein A. Controlling macro- and mesostructures with hierarchical porosity through combined hard and soft templating. Chem Soc Rev. 2013;42(9):3721-39.

[38] Soler-Illia GJdAA, Sanchez C, Lebeau B, Patarin J. Chemical Strategies To Design Textured Materials: from Microporous and Mesoporous Oxides to Nanonetworks and Hierarchical

Structures. Chemical Reviews. 2002;102(11):4093-138.

[39] Yang J, Peng J, Zou R, Peng F, Wang H, Yu H, et al. Mesoporous zinc-blende ZnS nanoparticles: synthesis, characterization and superior photocatalytic properties. Nanotechnology. 2008;19(25):255603.

[40] Rana RK, Zhang L, Yu JC, Mastai Y, Gedanken A. Mesoporous Structures from Supramolecular Assembly of in situ Generated ZnS Nanoparticles. Langmuir. 2003;19(14):5904-11.

[41] Zhang Q, Chi W, Zhang W, Lv C, Li J. Synthesis of surfactant-free self-assembled and size-controlled ZnS mesoporous nanospheres. New J Chem. 2012;36(1):119-24.

[42] Platschek B, Keilbach A, Bein T. Mesoporous Structures Confined in Anodic Alumina Membranes. Advanced Materials. 2011;23(21):2395-412.

[43] Yang C, An G, Zhao X. ZnS porous fluorescent nanostructures synthesized by a soft template approach. Journal of Materials Science: Materials in Electronics. 2015;26(5):3324-9.

[44] Zhu Y-P, Li J, Ma T-Y, Liu Y-P, Du G, Yuan Z-Y. Sonochemistry-assisted synthesis and optical properties of mesoporous ZnS nanomaterials. J Mater Chem A. 2014;2(4):1093-101.

[45] Mehta SK, Kumar S, Chaudhary S, Bhasin KK, Gradzielski M. Evolution of ZnS Nanoparticles via Facile CTAB Aqueous Micellar Solution Route: A Study on Controlling Parameters. Nanoscale Research Letters. 2008;4(1):17-28.

[46] Mistry B. A handbook of spectroscopic data. Chemistry. 2009.

[47] Khorsand Zak A, Abd. Majid WH, Abrishami ME, Yousefi R. X-ray analysis of ZnO nanoparticles by Williamson–Hall and size–strain plot methods. Solid State Sciences. 2011;13(1):251-6.

[48] Sidim T, Acar G. Alcohols Effect on Critic Micelle Concentration of Polysorbate 20 and Cetyl Trimethyl Ammonium Bromine Mixed Solutions. Journal of Surfactants and Detergents. 2013;16(4):601-7.

[49] Wan H, Xu L, Huang W-Q, Huang G-F, He C-N, Zhou J-H, et al. Band engineering of ZnS by codoping for visible-light photocatalysis. Applied Physics A. 2014;116(2):741-50.

[50] Hassanien AS, Akl AA. Influence of composition on optical and dispersion parameters of thermally evaporated non-crystalline Cd 50 S 50−x Se x thin films. Journal of Alloys and Compounds. 2015;648:280-90.

[51] Soltani N, Saion E, Hussein MZ, Erfani M, Abedini A, Bahmanrokh G, et al. Visible Light-Induced Degradation of Methylene Blue in the Presence of Photocatalytic ZnS and CdS Nanoparticles. International Journal of Molecular Sciences. 2012;13(12):12242-58.

[52] Purkayastha DD, Brahma R, Krishna MG, Madhurima V. Effects of metal doping on photoinduced hydrophilicity of SnO2 thin films. Bulletin of Materials Science. 2015;38(1):203-8.